SUPPORTING INFORMATION:

Optoelectronic characteristics of chemically processed ultra-thin $In_yZn_{1-y}O$ nanostructures

P. Ilanchezhiyan[a], C. Siva[b], A. Madhan Kumar[c], Fu Xiao[a], G. Mohan Kumar[a*]
and T. W. Kang[a]

[a]Quantum-Functional Semiconductor Research Center, Dongguk University, Seoul, Republic of Korea.
[b]Department of Physics and Nanotechnology, SRM University, Kattankulathur, India.
[c]Center of Research Excellence in Corrosion,
King Fahd University of Petroleum & Minerals, Kingdom of Saudi Arabia
Fax: +82-2-2278-4519; Tel: +82-10-4896-1777
Email: selvi1382@gmail.com, gmohankumar@dongguk.edu

Preparation of $In_{0.10}Zn_{0.90}O$ colloidal dispersion: Initially, 50 mg of $In_{0.10}Zn_{0.90}O$ was dispersed in 20 ml of methanol and sonicated for about 30 min and aged subsequently for another 6-12 h. Here, ageing process was ensured for the separation of larger particulates (*via* decantation) from the colloidal media. Two-three cycles were carried out similarly to procure a highly dispersed transparent colloidal dispersion (Fig. S7).

Characterization: The morphology and dimensions of the nanostructures were examined using a transmission electron microscope (JEOL JEM-2000EX2) and Hitachi S4800 (SEM). The phase purity and crystal structure of the processed materials were inferred using an X-ray RINT 2500 diffractometer with Cu Kα radiation (λ = 0.154 nm). Room-temperature Raman measurements were carried out using a Micro Confocal Raman spectrophotometer with an excitation wavelength of 514.5 nm. X-ray photoelectron spectroscopic measurements were carried out using a PHI 660 XPS spectrometer (using Al Kα radiation (1486.6 eV) as the excitation source). The absorbance spectrum was recorded using a Cary UV/VIS/ NIR spectrophotometer, while the room temperature emission properties were studied using a PL spectrophotometer with an excitation wavelength of 360 nm. The room-temperature current-voltage (*I*-*V*) characteristics were obtained using a Keithley 617 semiconductor parameter analyzer under dark and UV illuminated conditions.

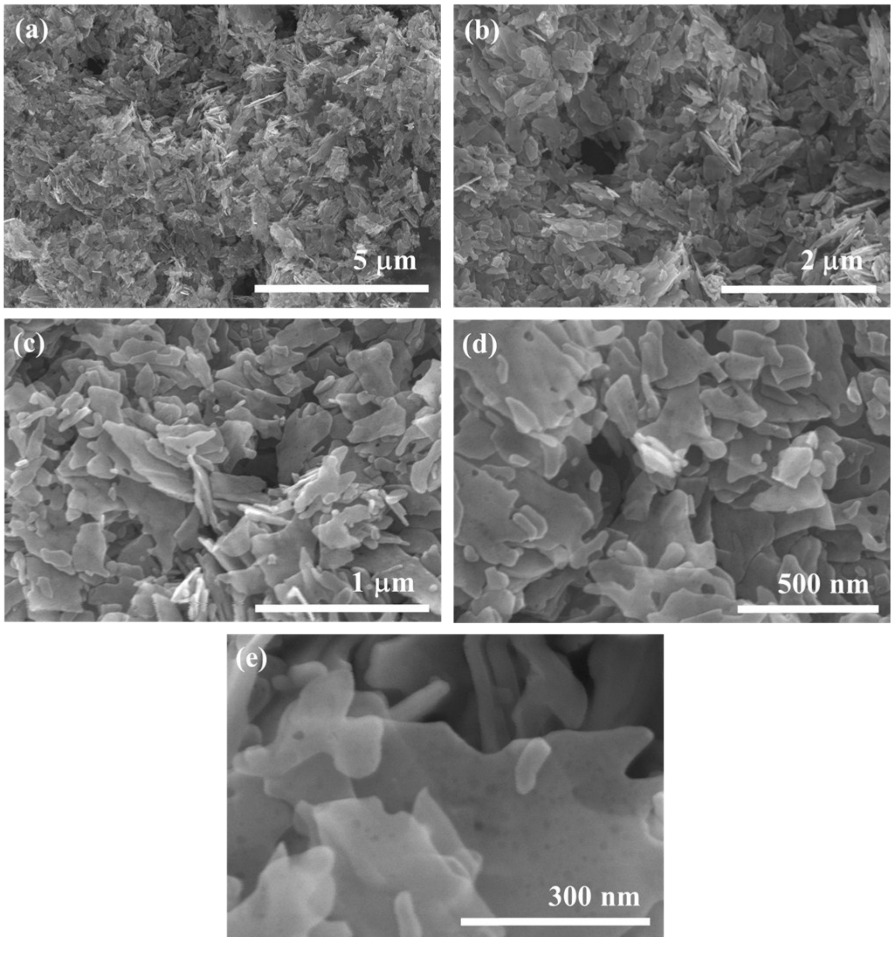

Figure S1: (a-c) Low-magnification SEM images of $In_{0.10}$ $Zn_{0.90}O$ nanosheets.

(d, e) High-magnification SEM images of $In_{0.10}$ $Zn_{0.90}O$ nanosheets.

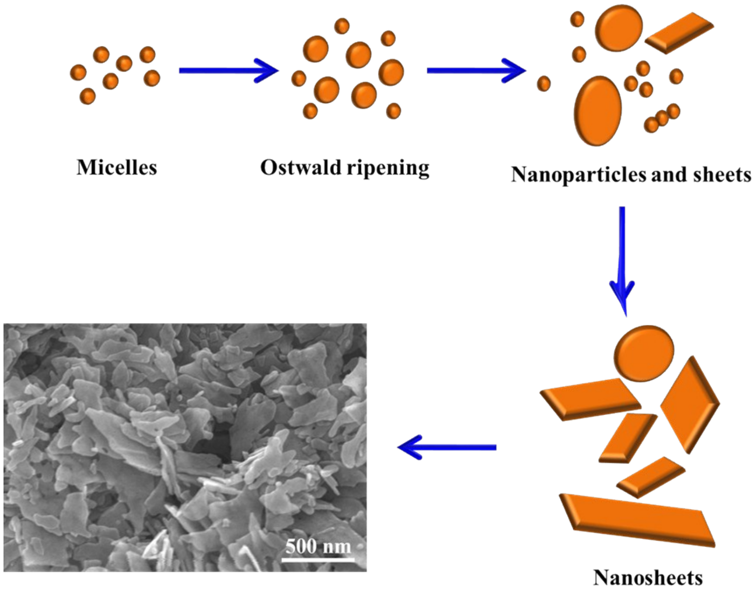

Figure S2: Schematic representation of the evolution of the sheet-like structures explained using Ostwald Ripening.

Growth mechanism of nanosheets: The morphological evolution of the sheet-like structures could be understood through the concept of Ostwald Ripening. According to the illustration shown in Figure S2, the smaller ZnO micelles in the precipitated solution get dissolved in the solvent to result with a supersaturated solution. Next, certain free molecules in the reaction mixture start to redeposit on the slightly larger particles to attain a thermodynamically stable state. This condition while prolonged results in the complete exhaustion of the smaller particulates to result with a large sheet-like configuration. This growth mechanism was also understood through the results obtained from the SEM measurements.

Morphology studies: The morphological appearance of $In_{0.01}Zn_{0.99}O$, $In_{0.03}Zn_{0.97}O$ and $In_{0.05}Zn_{0.95}O$ materials were studied using the aid of SEM. The analysis revealed the flake-like characteristics of the material, irrespective of In^{3+} composition. The dimension of the structures was also noted to be irregular in geometry and their representations are shown in Fig. S3.

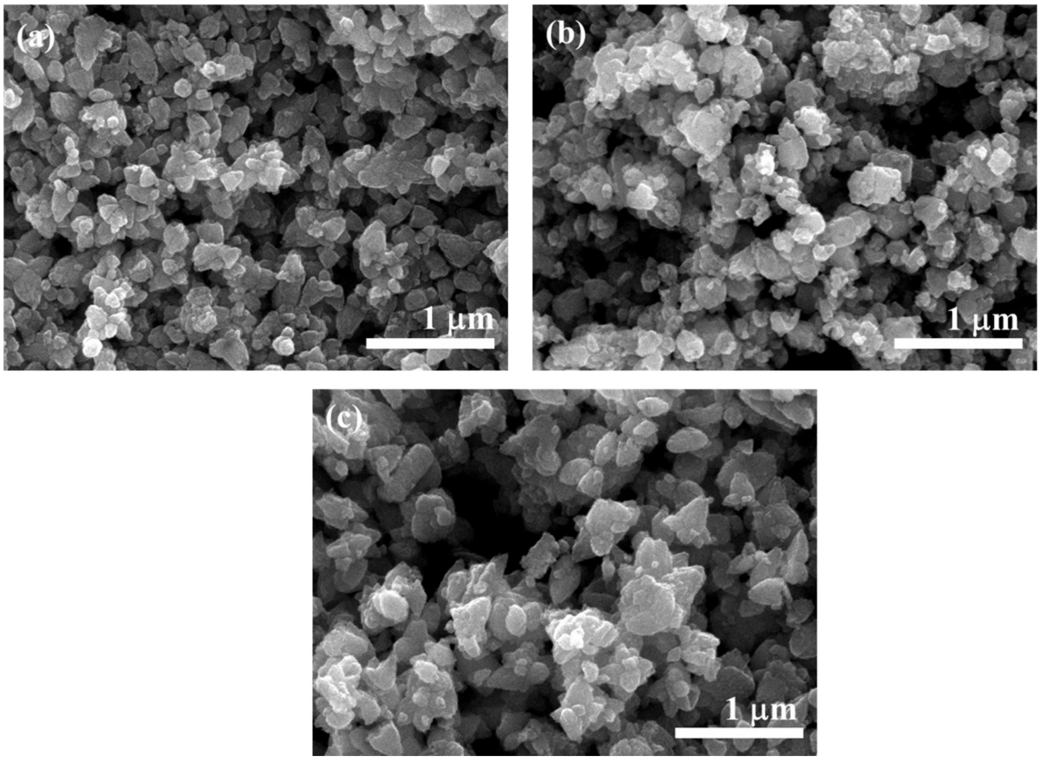

Figure S3: SEM images of (a) $In_{0.01}Zn_{0.99}O$ (b) $In_{0.03}Zn_{0.97}O$ and (c) $In_{0.05}Zn_{0.95}O$ nanostructures.

X-Ray diffraction results: Figure S4 shows the XRD patterns of undoped ZnO and various compositions of indium doped ZnO nanostructures. The diffraction patterns studied over a range of $30 < 2\theta < 70°$ were noted to be well indexed to the wurtzite ZnO and signify the samples to be well crystallized and agree with the standard card (JCPDS 36-1451). Interestingly, the (101) peak position of $In_yZn_{1-y}O$ nanostructures was observed to shift slightly towards the lower angles, which usually corresponds to the increase in c value. This shift could also be attributed to the greater extent of In^{3+} incorporation into the wurtzite matrix, as their radius (0.080 nm) is considerably larger than that of the Zn^{2+} ion (0.074 nm) [R1]. We would also like to add that the existence of indium hydroxide secondary phase characteristics was noted in the $In_{0.10}Zn_{0.90}O$ systems alone.

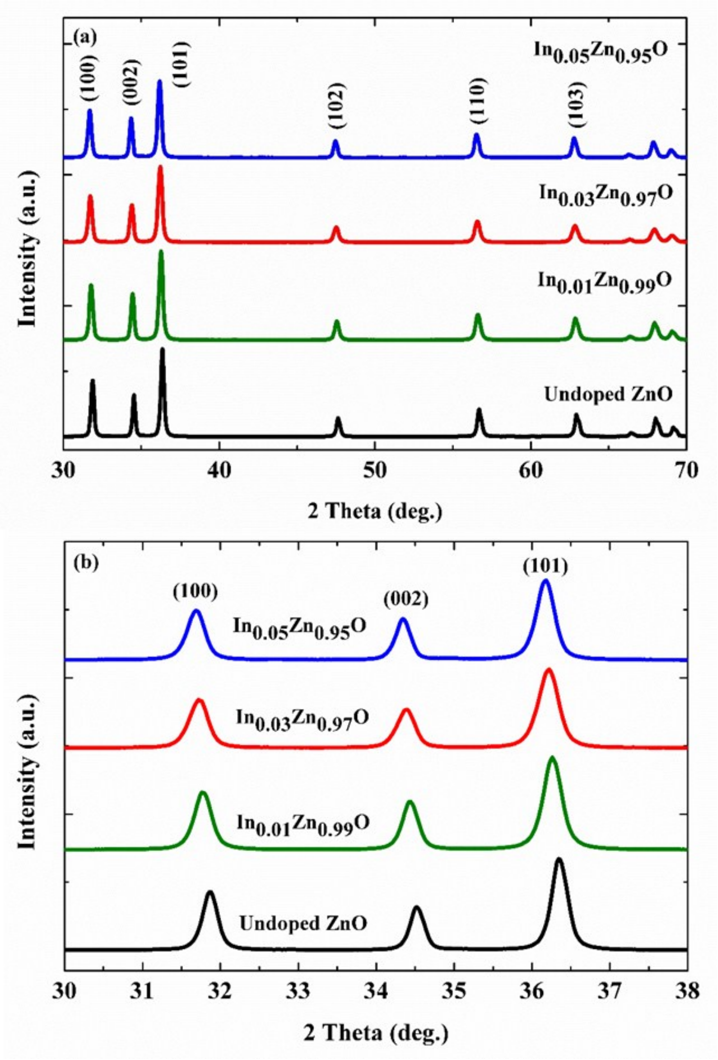

Figure S4: (a) XRD patterns of undoped ZnO and $In_yZn_{1-y}O$ nanostructures. (b) The shift in (101) peak position towards the lower angles with respect to the increase in In^{3+} composition.

Raman measurements: The room-temperature Raman measurements revealed the E_1 (LO) mode of undoped ZnO (≈584 cm^{-1}) to be less predominant on par with that of the $In_yZn_{1-y}O$ nanostructures (Fig. S5). Generally, E_1 (LO) mode in ZnO is related to the existence of intrinsic defects such as Zn interstitials (Zn_i) or O vacancies (V_O) [R2, R3]. So, the improved intensities of E_1 (LO) in the present study signify the increased defect densities in the processed nanostructures. And this could be attributed to the increased substitution of dopant ions in the wurtzite ZnO lattice, as they could have induced certain vibrations in the O related sub lattices and resulted with the observed characteristics. The spectra also reveal a small broader shoulder like structure to emerge around 535 cm^{-1} in the doped materials. This vibration could be related to the A_1 symmetry and attributed to the $2B_1$ low and LA overtones along L, M and H lines [R4].

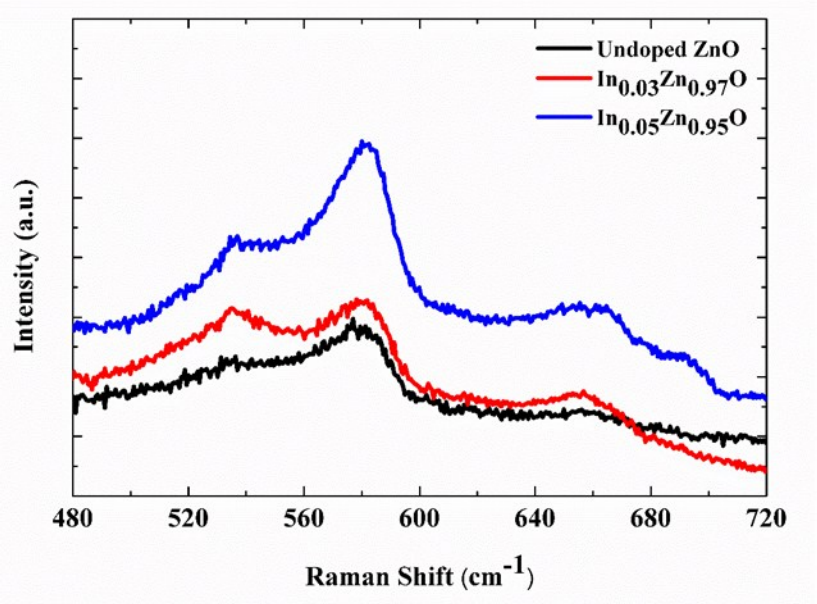

Figure S5: Raman spectra of the undoped ZnO and $In_yZn_{1-y}O$ nanostructures revealing the increase in oxygen related defects on increased dopant substitution.

Energy dispersive spectroscopic (EDS) measurements: The compositional details of the various elements existing within the $In_{0.10}Zn_{0.90}O$ nanostructures were estimated using EDS measurements. Here, the atomic percentage of Zn, In and O ions was estimated to be around 51, 6 and 43 %, respectively. The measurements were actually carried out over three-five different regions to estimate the average values. The EDS spectra are shown in Figure S6 for reference.

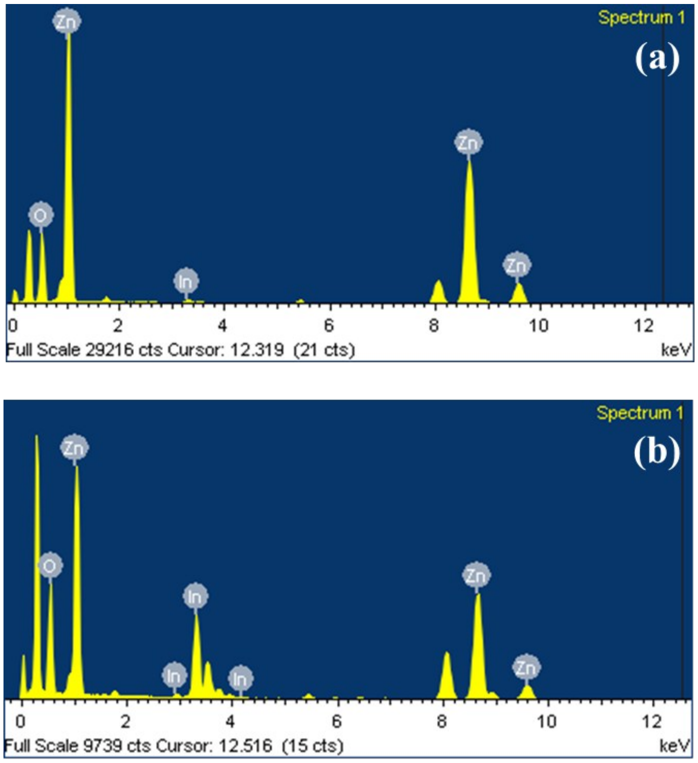

Figure S6: EDS spectra of $In_{0.03}Zn_{0.97}O$ and $In_{0.10}Zn_{0.90}O$ nanostructures.

Figure S7: Highly dispersed/transparent $In_{0.10}Zn_{0.90}O$ colloidal dispersion.

UV-vis absorbance measurements: The influence of In^{3+} ions on the optical band gap (E_g) of ZnO was investigated using UV-vis absorbance measurements. Figure S8 reveals a significant enhancement in the absorbance values of undoped ZnO towards the visible region (as a function of In^{3+} composition), along with a significant red shift in their corresponding absorption band edges. The shift in band edge also signifies the shift in E_g values, which could be reasoned with the sp-d exchange interaction between band electrons and the localized d electrons of indium ions substituting at the Zn sites [R5]. Similarly, the modification in lattice dynamics of ZnO that takes place on indium incorporation could also be reasoned for the observed red shift.

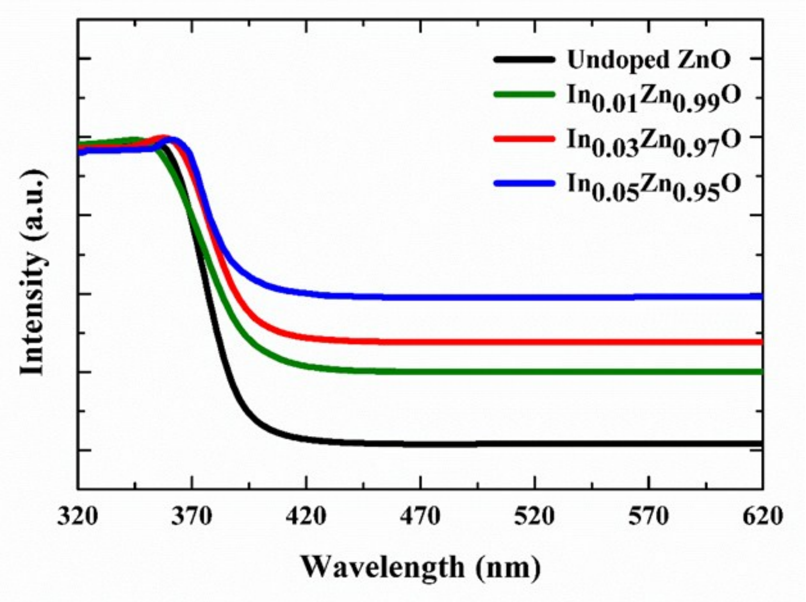

Figure S8: UV-vis absorption spectroscopic analysis of the undoped ZnO and $In_yZn_{1-y}O$ nanostructures revealing the red shift in absorption edge.

Photoluminescence (PL) measurements: The room-temperature PL spectra shown in Fig. S9 demonstrates the occurrence of emissions across ultra-violet and visible region for $In_yZn_{1-y}O$ nanostructures. The UV emissions could be related to the near-band edge (NBE) emissions in ZnO, while the latter with the sub-band edge (SBE) emissions. As SBE emissions in ZnO are usually correlated with the influence of defects; their enhanced emissions in $In_yZn_{1-y}O$ could be regarded as substantial evidence that signifies the increased defect densities on increased In^{3+} substitution in the host matrix [R6, R7].

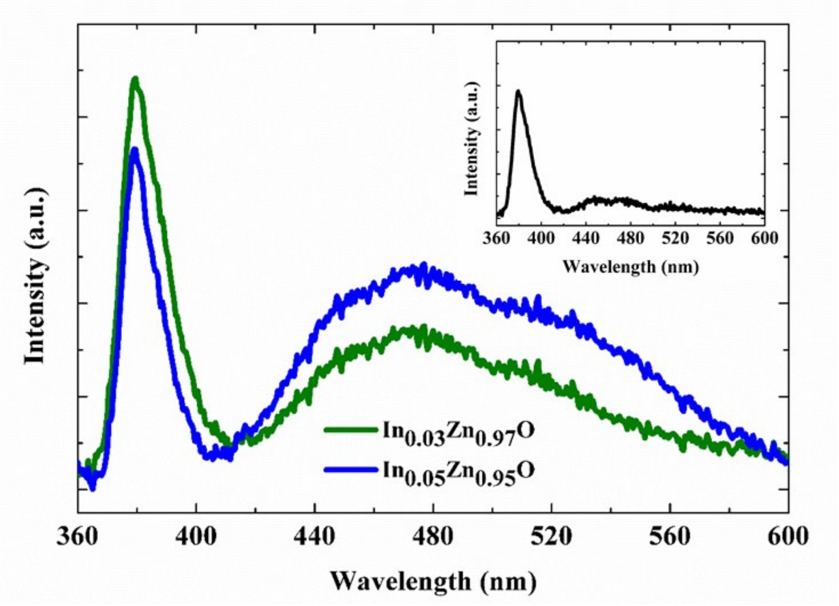

Figure S9: PL spectra of $In_yZn_{1-y}O$ nanostructures revealing the enhancement in defect related emissions along the visible region. Inset corresponds to the PL spectrum of undoped ZnO.

Mott-Schottky plot: Mott-Schottky (MS) plots are generally used to determine the nature of doping type, apparent donor density (N_D) and the flat band potential (V_{FB}). The slopes determined from the analysis of MS plot (Fig. 3a) were actually used to estimate their corresponding carrier density (N_D)

$$N_D = (2/ e_0\varepsilon\varepsilon_0) [d (1/C^2)/dV]^{-1}$$

where e_0 is the electron charge, ε the dielectric constant of ZnO, ε_0 the permittivity of vacuum, N_D the dopant density. Using the above formula the carrier density was calculated for the obtained material [R8].

Current-Voltage (I-V) characteristics: Figure S10 shows the *I-V* characteristics of different combinations of p-n junctions (fabricated using different compositions of In^{3+} doped ZnO) under dark conditions. *I-V* results were actually obtained after establishing appropriate contacts using silver paste. The initially observed rectifying behaviour in the fabricated heterostructures substantiates the formation of *p-n* junction across the corresponding interfaces. The improved current values as a function of In^{3+} composition values signifies the importance of arriving at the present structure for efficient photodiode related applications. Similarly, the increased leakage current under negative potential could be attributed to the increase in resistance values (resulting from the random aggregates distributed cross the hybrid architecture) and the existence of surface defects present in $In_yZn_{1-y}O$ nanostructures [R9].

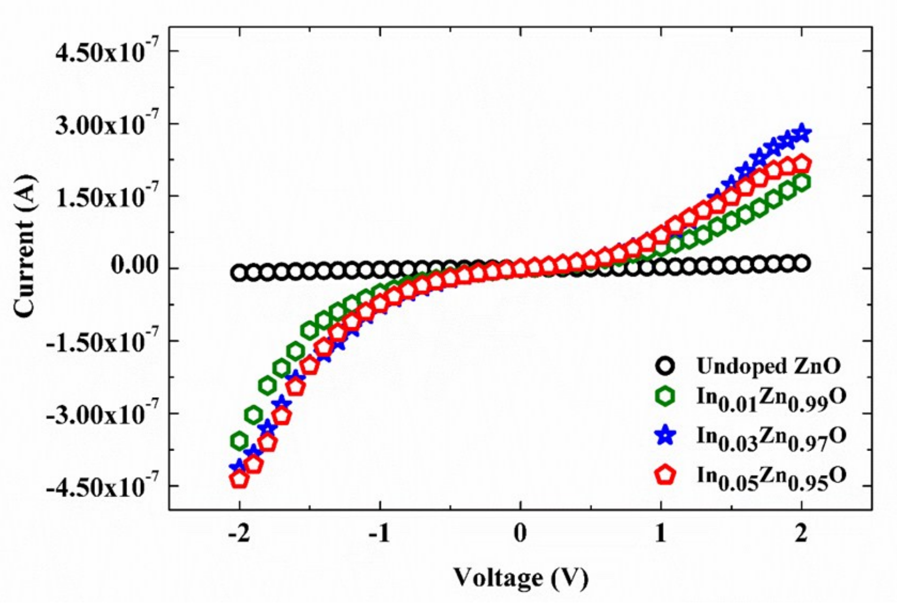

Figure S10: *I-V* characteristics of *p*-Si/*n*- $In_yZn_{1-y}O$ heterojunctions in linear scale.

References:

R1. Sumati Pati, P. Banerji and S. B. Majumder, RSC Adv., 2015, **5**, 61230; Y. W. Chen, Y. C. Liu, S. X. Lu, C. S. Xu, C. L. Shao, C. Wang, J. Y. Zhang, *J. Chem. Phys.*, 2005, **123**, 134701.

R2. T. C. Damen, S. P. S. Porto and B. Tell, *Phys. Rev.*, 1966, **142**, 570-574.

R3. D. F. Zhang, L. D. Sun, C. H. Yan, *Chem. Phys. Lett.*, 2006, **422**, 46-50.

R4. Tamil Many K. Thandavan, Siti Meriam Abdul Gani, Chiow San Wong and Roslan Md Nor, *J. Nanomater.*, 2014, **2014**, 105875.

R5. W. K. Liu, G. Mackay Salley and D. R. Gamelin, *J. Phys. Chem. B*, 2005, **109**, 14486.

R6. Y. Sun, N. G. Ndifor-Angwafor, D. J. Riley and M. N. R. Ashfold, *Chem. Phys. Lett.*, 2006, **431**, 352.

R7. L. Wu, Y. Wu, X. Pan and F. Kong, *Opt. Mater.*, 2006, **28**, 418.

R8. S. Mridha and D. Basak, *Appl. Phys. Lett.*, 2008, **92**, 142111.

R9. Iván Mora-Seró, Francisco Fabregat-Santiago, Benjamin Denier, Juan Bisquert, Ramón Tena-Zaera, Jamil Elias, Claude Lévy-Clément, *Appl. Phys. Lett.*, 2006, **89**, 203117.